X-ray studies of interlayer water absorption and mesoporous water transport in a weakly hydrated clay

H. Hemmen, L. R. Alme, Jon Fossum, Yves Méheust

X-ray studies of interlayer water absorption and mesoporous water transport in a weakly hydrated clay

H. Hemmen,[1,*,†] L. R. Alme,[1] J. O. Fossum,[1,*,‡] and Y. Meheust[2]
[1]*Department of Physics, Norwegian University of Science and Technology, Hoegskoleringen 5, N-7491 Trondheim, Norway*
[2]*Geosciences Rennes, UMR CNRS 6118, Université de Rennes 1, Rennes, France*
(Received 10 May 2010; published 20 September 2010)

The swelling of layered smectite clay particles consists of a change in the interlayer repetition distance (*d*-spacing) as a function of temperature and humidity. For the synthetic clay sodium fluorohectorite, hydrodynamically stable hydration states with zero, one and two intercalated monolayers of water have previously been reported, with discrete jumps in *d*-spacing at the transitions between the hydration states. Keeping the temperature fixed and varying the ambient relative humidity, we find small reproducible *d*-spacing changes also *within* the hydration states. These changes are monotonous as a function of relative humidity, and one order of magnitude smaller than the shift in *d*-spacing that is typical of the transition between two hydration states. The reproducibility and reliability of this relative humidity controlled *d*-shift enables us to use the interlayer repetition distance *d* as a measure of the local humidity surrounding the clay particles. We provide an example of application of this observation: imposing a humidity gradient over a quasi-one-dimensional temperature-controlled sample, and using x-ray diffraction to record the *d*-spacing, we are able to extract profiles of the relative humidity along the sample length. Their time evolution describes the transport of water through the mesoporous space inside the clay. An analysis of the measured humidity profiles based on the Boltzmann transformation, under certain simplifying assumptions, yields a diffusive behavior that is either normal or possibly weakly anomalous.

DOI: 10.1103/PhysRevE.82.036315 PACS number(s): 47.56.+r, 81.05.Rm, 78.70.Ck, 71.20.Tx

I. INTRODUCTION

Swelling clays are widespread in soils and sedimentary rock basins and play an important role in many environmental and industrial processes, such as in the petroleum industry for engineering and catalysis. Layered smectite clays have a nanoporous structure that water and organic compounds may intercalate into. The interlayer hydration/dehydration may play a key role, in e.g., subsurface fluid migration, damage to buildings, oil well stability [1], as well as for the stability of land clay formations [2]. Current interests for applications are e.g., within membrane technology and control of contaminant transport in clay-containing ground formations, relevant for capping of nuclear waste [3] and CO_2 storage reservoirs [4].

The small particle size and microporous structure of clays [5] give them the capability to absorb water. Smectite clay particles are made up of stacked crystalline layers. These decks of cards are held together by charge balancing cations in the nanoscale interlayer spacing [6]. As water intercalates between layers, the number of intercalated water molecules and their molecular packing arrangements are dependent on relative humidity and temperature [7,8]. The various interactions between the interlayer cation, the absorbed water molecules, and the charged silicate surface, lead to static structural properties and complex hydration dynamics that are still not well understood.

The sodium fluorohectorite (NaFh) clay used in this study is a phyllosilicate (sheet silicate) in which several 2:1 elementary crystalline lamellae or platelets stack together to form quasicrystalline particles/grains, which contain 80–100 platelets on average [8–11]. NaFh is a synthetic and chemistry customized clay mineral, which differs from "normal" hectorite by the substitution of hydroxyl groups with fluorine ions (F^-). NaFh has a rather large surface charge of −1.2 e/unit cell, originating from the substitution of Li^+ with Mg^{2+} in the octahedral layer [12]. It also exhibits a fairly large and variable particle size ranging from a few nm up to ≈10 μm in diameter, and it is expected to display a more homogeneous composition and charge distribution in comparison to naturally occurring clays [10,13]. The particle thickness of about 80–100 platelets corresponds approximately to 0.1 μm, which implies that even though the individual platelets are stacked in relatively large numbers, the resulting particle has a diameter-to-height ratio close to 100:1.

The stacking of layers creates a regular van der Waals gap between them—often called the *interlayer space* or *gallery*—which for NaFh is occupied by sodium cations. Insertion of guest species into the quasi two-dimensional host galleries is facilitated by the characteristic strong intralayer and weak interlayer bonding in the host lattice. Thus, intercalation of various molecules, even polymers, between the layers is facile; and in the case of the present study, the hydration of the intercalated sodium cations is of particular interest.

While all clays adsorb water (onto the outside grain surfaces), they do not necessarily absorb water into the crystalline or grain structure. Whether or not a clay mineral of the present type undergoes swelling—i.e., an increase in particle thickness due to water intercalation between the platelets—depends on the layer charge and the contributing Coulomb interaction between guest cations and host layer [12].

*Corresponding author.
†henrik.hemmen@ntnu.no
‡jon.fossum@ntnu.no

For NaFh, three hydrodynamically stable hydration states at ambient humidity are reported: they are characterized by particular values of the repetition distance of platelets inside the grains, namely ≈10 Å, ≈12.5 Å, and ≈15 Å, and are denoted as zero water layers (0 WL), one water layer (1 WL), and two water layers (2 WL) [7,8,10], respectively. These states are also referred to, respectively, as dehydrated, monohydrated, and dihydrated. Intercalation beyond two water layers is inhibited by the high surface charge of the clay layers. In addition, the Pauling radius of the intercalation cation is assumed to be an important contribution factor for explaining the limitations of crystalline swelling [14].

The classical approach of treating interlayer water as discrete, static layers is an approximation that to some extent hides some of the interesting physics that can be found in the subangstrom scale changes within a given hydration state. Thus a more nuanced picture of the interlayer dynamics, and the interplay between the nanopores and mesopores, is investigated experimentally in this paper. The key approach has been to keep in sight that behind the simplified description in terms of discrete water layers, there are molecular packing effects. This aspect has been treated theoretically in several articles on Monte Carlo simulations and other simulations where the physics at a molecular level is addressed and not just concealed within macroscopically averaged variables (see e.g., [15–18]). The same packing effects are also observed through NMR-measurements [19].

When dry clay powder is subjected to a humid environment, water or water vapor penetrates the pore space of the powder, which exists at several length scales: first the clay's ability to intercalate guest ions and water molecules creates sub 10 nm *nanopores* between the platelets; second there are *mesopores* of intermediate (micrometer) order between adjacent particles. Under varying humidity in the mesopores, the extent of the nanopores changes due to the surrounding vapor pressure in the mesopores. In this process, the crystalline configuration of the basal clay sheets remains constant, while the interlayer distance between the sheets changes. In the current study, we use x-ray diffraction to measure the continuous changes in interlayer repetition distance d as a function of relative humidity (H), and show that the changes are reproducible. We also present an application of this d-to-H relation, consisting in using the x-ray recordable interlayer spacing to monitor water transport through the mesopores.

II. EXPERIMENT

A. Samples and equipment

Sodium fluorohectorite clay was prepared from synthetic Li-fluorohectorite (Corning Inc., New York) by an ion-exchange process producing pure sodium fluorohectorite powder. A thorough description of this process can be found in Lovoll *et al.* [10]. The obtained clay crystallites have the nominal chemical formula Na_x-$(Mg_{3-x}Li_x)Si_4O_{10}F_2$ (per half unit cell) [8]. To minimize large clusters of particles, the sample was ground thoroughly into a fine powder.

The x-ray scattering experiments were conducted at the Norwegian University of Science and Technology (NTNU) utilizing NanoSTAR, a small-angle x-ray scattering system from Bruker AXS. The scattered intensity was recorded with a two-dimensional multiwire gas detector, mounted at a distance that allowed recording of wide angle scattering (WAXS). The x-ray wavelength was 1.54 Å, with a beam size of 400×400 μm^2. The available q-range for this experiment was $0.7\ nm^{-1}<q<7.7\ nm^{-1}$. A goniometer in the sample chamber provided precise and reproducible sample translation in the xz plane, perpendicular to the incoming beam, as well as rotation about the vertical z axis (φ-angles).

To control the temperature, an autotuning temperature controller including a heater was employed, together with a Peltier element and a variable temperature heat sink (applicable for cooling). We also used a setup for hydration control, based on controlled air flow over the (immediate) surface of a saturated solution of a K_2SO_4 salt. The salt solution's affinity for water regulates the partial vapor pressure of water above the solution. This partial pressure is a constant at a fixed particular temperature and can be found tabulated in the literature (see, e.g., [20]). Finally a peristaltic pump provided air circulation throughout the system, and a temperature probe was used to measure relative humidity and temperature of the circulating air.

Two different types of experiments were performed. The first consisted in mapping small displacements of the (001) Bragg peak positions as a function of the humidity imposed on a powder sample at fixed temperature. In the second type of experiment we studied the ingress of water vapor through a powder-filled capillary. The results of the first experiment were employed in the data analysis of the second, in order to infer local values of relative humidity from the scattering data. The experimental methods and sample cells are presented below.

B. Diffraction from the clay powder

In our powder sample, the particles are randomly orientated in the scattering volume. Because the dominating x-ray crystallographic direction of the NaFh particles is perpendicular to the stacked platelets, only a fraction of the particles will have the correct orientation for Bragg scattering to occur. Bragg's law of diffraction in this case is $2d_{001}\sin\theta=\lambda$, where d_{001} is the repetition distance between adjacent clay layers, and λ is the x-ray wavelength. The resulting Debye-Scherrer cone has apex half angle 2θ resulting in a ring of interference on the detector with radius given as $r\sin 2\theta$ (Fig. 1). The scattering angle θ is the angle of incidence on the platelets with respect to the 001 orientation and r is the sample to detector distance. The recording of powder diffraction data with a two-dimensional detector implies that all the statistics are included in one scan frame, i.e., all particle shape and size variants as well as particle angular distributions.

C. Bragg scattering vs humidity level around the scatterers

A small amount of powder sample was placed inside a cylindrical hole of diameter 1.0 mm and thickness 1.5 mm in a piece of copper. We kept the amount of sample limited for three reasons: primarily to keep the transmission of the x-ray radiation high, as this is effectively attenuated by the clay,

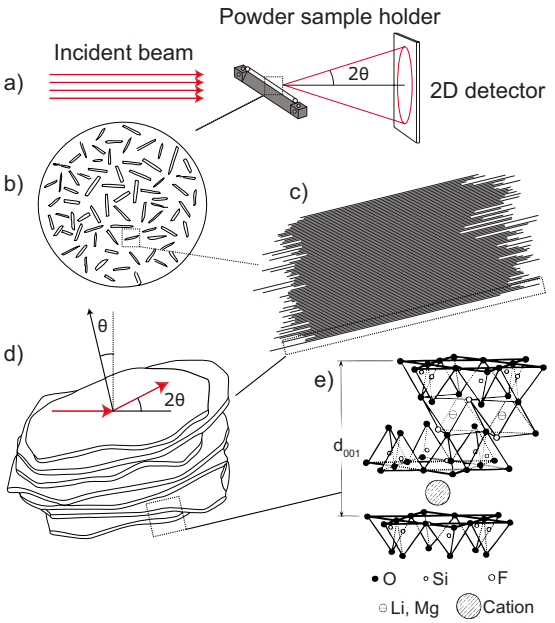

FIG. 1. (Color online) Schematic illustration of the scattering geometry. (a) The incident beam is scattered from a powder sample with randomly orientated particles, resulting in a Debye-Scherrer scattering pattern on the 2D detector. (b) Cross-section of the capillary containing randomly oriented clay grains. (c) Micron-scale clay particle formed from stacked lamellae. (d) Layer configuration inside the particle grain. The angle between the incident beam and the 001 normal vector from a scattering particle is θ, hence the scattering angle is 2θ. (e) Generic structure of fluorohectorite synthetic clay.

second to avoid multiple scattering, and third to ensure a fast response with respect to changes in temperature and/or humidity. The geometry of the sample cell ensured good thermal contact between the sample and the sample holder, while at the same time exposing a relatively large surface to the surrounding humidity. A "roof" covering the sample holder prevented any possible condensation directly on the clay surface. The base of the sample cell was made of copper for good thermal conduction, and precise temperature control was done by a LakeShore temperature controller in conjunction with a Peltier element and a variable temperature heat sink.

To vary the humidity inside the sample container, we utilized the open circuit humidity regulator illustrated in Fig. 2(a). To produce dry air, a columnar container filled with silica gel was used. Filtrating air through the gel effectively reduces the relative humidity of the air to approximately 3%. To produce humid air, a chamber of saturated solution of K_2SO_4 salt was employed, for which the relative humidity of the air at its interface with the solution, at room temperature, is tabulated to 97% [20]. To achieve continuous control of relative humidity over the entire humidity interval, we applied two separate pumps and two open circuits, which after passing through the silica gel and salt chamber respectively were joined into one circuit passing over the sample. By varying the air flow in the two pumps, and thereby the volume ratio of dry and humid air in the joined circuit, we were able to vary the relative humidity imposed on the sample.

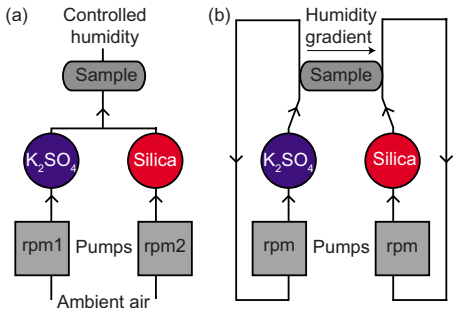

FIG. 2. (Color online) (a) Schematics of the open air humidity circuit setup. Ambient air is passed through two separate circuits, one through a column of silica gel desiccant and the other over the surface of a K_2SO_4 salt solution. The joined air-flow is passed through the sample holder, and the humidity of the sample environment is controlled by regulating the air flows (rpm1 and rpm2) of the two initially wet and dry circuits. (b) Schematics of the closed air humidity circuit setup. Instead of circulating ambient air, both air flows are kept in closed loops with approximately equal flow due to the same rounds per minute (rpm) of the peristaltic pumps. By passing one circuit at one side of the sample and the other circuit at the other side, a humidity gradient is imposed over the sample length. The arrows indicate the direction of the air flow.

To keep the circulating air at the same temperature as the sample itself, the air flow was passed through copper foam kept at the sample temperature for temperature heat exchange. A humidity and temperature probe was attached through a lead-in aperture in the container ceiling. The humidity probe was calibrated prior to the experiment using saturated solutions of NaCl and LiCl, and checked against a solution of K_2SO_4 producing an error margin of $\pm 0.3\%$ RH. Finally, windows of x-ray transparent kapton on opposite sides of the cylindrical aluminum container enabled free passage for both the incoming x-ray beam and the scattered x rays.

The experiment was initiated by lowering the temperature to 15.0 °C at ambient humidity. The d-spacings for stable configurations were then measured from the x ray scattering diffractograms while varying the relative humidity by steps; first by increasing H toward H_{max}, then by lowering it down to H_{min} and finally by increasing it again back to $H_{ambient}$. This procedure was then repeated. Each data acquisition lasted 30 min in order to keep a good signal-to-noise ratio. A rough data analysis was performed simultaneous with the data acquisition, which showed that the average d-spacing measured in the scattering volume stabilized during the first scan-time after stepping up or down the humidity. To ensure that equilibrium was reached, a minimum of five consecutive scans were still carried out at each humidity level, and the humidity was never varied in steps larger than a few percent. Furthermore, the assumption of equilibrium was verified by measuring the d-spacing at a particular value of H and then next increasing the humidity by an amount ΔH, still remaining within the same water-layer hydration state. By subsequently returning the system to the original H, i.e., decreasing the humidity by the same amount ΔH, we obtained the exact same d-spacing. This procedure is not valid if one changes between hydration states, due to hysteresis effects.

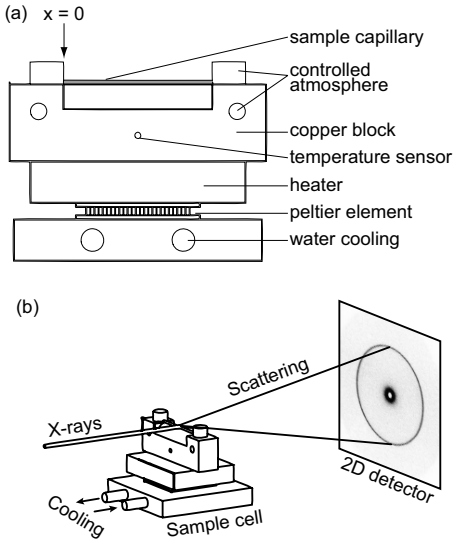

FIG. 3. Sample cell for observing the water ingress through the interlayer spacing. (a) Schematic of the sample cell. (b) Scattering geometry.

In order to ensure equilibrium conditions at humidities around the transition point, even more scans were acquired at humidity levels close to and within the transition region between hydration states.

To check reproducibility, we carried out the experiment on three different powder samples. In total, three experiments of about 700–800 scans were performed in order to map the peak dynamics as a function of varying relative humidity.

D. Humidity transport

We studied the humidity transport through NaFh powder placed in a glass capillary (1.0 mm diameter, 80 mm length, wall thickness 0.01 mm) perpendicular to the incident x-ray beam. Prior to filling the capillary, the powder was thoroughly ground, in order to break up large particle aggregates and minimize macropores. By macropores we mean pores created by packing the powder in the capillary; the resulting pores are larger than a typical particle size. Assuming that no macropores exist in our samples, water transport occurs only through nano- and mesopores in the medium. Among these, the main structures where water transport takes place are the larger mesopores. However, the nanoporous structure could influence the water transport in the mesopores, due to the fact that the swelling property directly modifies the structure of the mesoporous space, and also removes some of the diffusing water (possibly acting as a limited sink). The 1 mm diameter of the glass capillary means that the sample volume exposed to the x-ray beam is in all cases comparable to that in the peak displacement experiment described in Sec. II C. The open-ended capillary was mounted with thermal paste on the sharp top edge of a copper block. A schematic illustration is shown in Fig. 3. The capillary was filled only so much as to ensure that the clay front exposed to humid air would lie outside the x-ray obstructing copper lids. This enabled observation of water vapor ingress already from the very edge of the sample ($x=0$).

A humidity gradient was imposed across the sample by exposing the two open ends of the capillary tube to the circulating air of two separated dry and humid air-flow circuits. A schematic outline of this setup is shown in Fig. 2(b). A double pump head attached to a single pump enabled almost equal flow in the two circuits, which was important to avoid any pressure gradients over the sample. The repeated circulation of the closed circuits was an aid in getting the air either very dry or very humid. We measured the relative humidity of the circulating air on both sides by hygrometers prior to the air passing through the sample. The temperature control system employed for this setup was the same as for the peak displacement experiment in Sec. II C.

Before initiating the experiment, the transmission of the x-ray beam was measured throughout the capillary. Peaks in the transmission values would indicate air pockets that could influence the results. As that was not the case, the packing of the clay powder was found to be sufficiently homogenous. The capillary was next mounted on the sample holder, and the goniometer φ-angle was adjusted so that the radius of the scattering cone measured on the detector be consistent over the entire length of the sample. This ensured sample orientation parallel to the detector (perpendicular to the beam).

The experiment was initiated by lowering the temperature to 15.0 °C, and waiting 5 min for thermal equilibrium to be reached. The humidity gradient was then imposed on the sample, which marked the start of the experiment ($t=0$). At the humid side, water vapor penetrates the sample by diffusing through the pore space between the clay particles. The pore space vapor concentration thereby increases and water intercalates into the interlayer spacing. This manifests itself on the x-ray detector as changes in the scattering patterns from the clay crystallites. We studied the dynamics of diffusion by studying the scattering profiles at different times and distances from the humid side of the sample.

The acquisition time was set to 15 min, in order to ensure a temporal resolution sufficient to map the dynamics. Although the scan time was reduced compared with the experiment on peak displacement that we have presented in Sec II C, and therefore resulted in a poorer signal to noise ratio, it was still well within the limit for successful data analysis. Over the course of the experiment, the sample was repeatedly scanned horizontally in increments of 1.0 mm. In total, 808 consecutive scans were performed.

Since glass capillaries are known to be quite *hydrophilic*, that is, attract water, we performed a second experiment identical to the experiment explained above, in order to investigate whether capillary flow on the glass surface affects the humidity transport. Silica surfaces are known to exhibit up to about 8 μmol/m^2 of hydroxyl groups, which corresponds to about 4.6 hydroxyl groups per 10 nm^2 of glass [21]. This high density results in a strong attraction of water molecules. To reduce the effect of hydrophilicity and capillary flow, the glass surfaces can be made *hydrophobic* through a *silanization* process, in which the free hydroxyl groups are made to react with a silicon compound, causing the water to be repelled from the surface, instead of bonding with it.

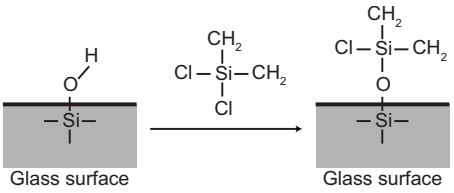

FIG. 4. Silanization of hydrophilic glass surface with reactive chlorosilane.

We adapted a method from Ref. [21] suggesting silanization by vapor treatment as the best method for silanization of glass. Hence a small amount of silanization reagent [silanization solution 1 from Sigma-Aldrich: ≈5% dimethyldichlorosilane ($C_2H_6Cl_2Si$) in heptane] was injected at the open ends of glass capillaries, which were next turned upside down and put in a beaker inside a sealed-off environment. The beaker with the samples was heated at 200 °C for about 1 h. During this time, the silicon compound evaporates and is expected to bind covalently to the free hydroxyl groups of the glass (Fig. 4).

A check on the efficiency of the silanization procedure was done by comparing the contact angle in a silanized capillary with that of a non-treated one. The results shown in Fig. 5, clearly indicate that the silanization process was successful.

To check whether the hydrophilicity of the capillaries had any impact on humidity transport, we used a sample holder designed for conducting scans on six capillaries simultaneously. Three of the capillaries were silanized, and three were left untreated. There were six 0.8×50 mm^2 slits cut out of a copper block for transmission of the diffracted beam, and a channel at each side for air flow. The capillaries were mounted with thermal paste over the slits, and every other capillary was silanized and untreated. The alternating arrangement was chosen to avoid misinterpretations that could arise from potential temperature or humidity gradients over the sample holder.

In order to get frequent scans on all six capillaries, the acquisition time was set to 5 min, which implies a significant lowering of the signal-to-noise ratio compared to the single capillary setup. However, it proved to be within reasonable limits, because the focus of this specific experiment was to trace the ingressing *intercalation front*, and not constantly mapping the humidity gradient across the sample.

A scan series of 954 consecutive scans was performed, where the intercalation front in all six capillaries was traced

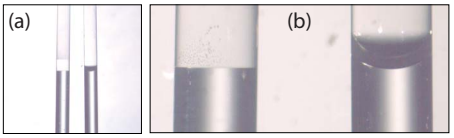

FIG. 5. (Color online) Micrographs of one silanized and one nontreated glass capillary with diameter 1 mm and wall thickness 0.01 mm. (a) The capillary to the left was treated with a silanization solution, whereas the one to the right was nontreated. Note the difference in contact angle; the water is clearly attracted along the glass walls of the nontreated capillary. Conversely, the water surface in the treated capillary is almost flat and sharp. (b) Magnification of the water-air interface.

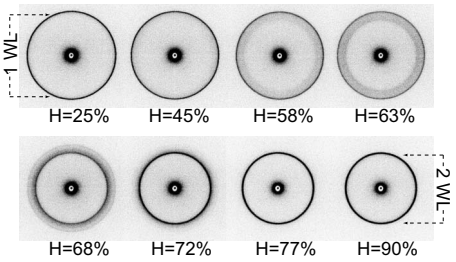

FIG. 6. Photo series of Debye-Scherrer scattering rings at various relative humidities.

with a longitudinal spatial increment of 0.5 mm. The humidity and temperature controls utilized were equal to what has previously been described for the single capillary case.

III. DATA ACQUISITION AND PROCESSING

Examples of two-dimensional diffractograms recorded as a function of humidity are shown in Fig. 6. For each of the experiments, all of the individual scan frames were radially integrated along conic line segments.

Due to small-angle scattering from the clay powder, background scattering decaying with increasing scattering angle is superimposed on the Debye-Scherrer cones; it is clearly visible in plots of the integrated intensity [Fig. 7(a)]. In ad-

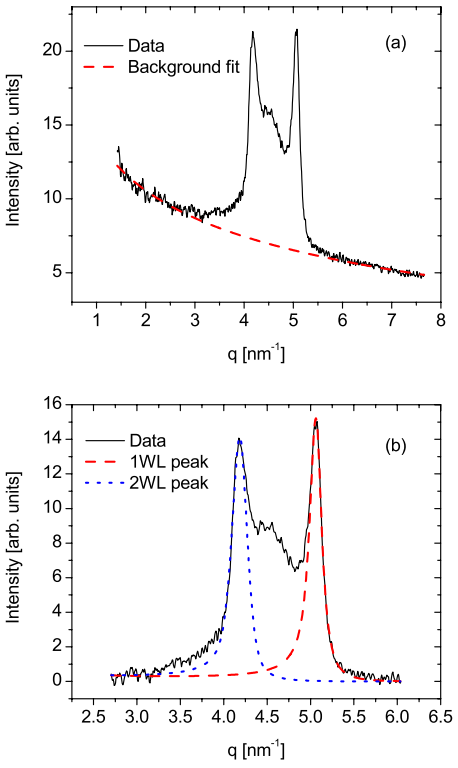

FIG. 7. (Color online) (a) The background noise is fitted to a power law and subtracted from the data. Note that the noise is considerable for low angles, but this region is not important for the data analysis. (b) Pseudo-Voigtian peak fit. The fitted peaks have been multiplied by the $|G(q)|^2 L_p(q)$ factors for comparison to the data.

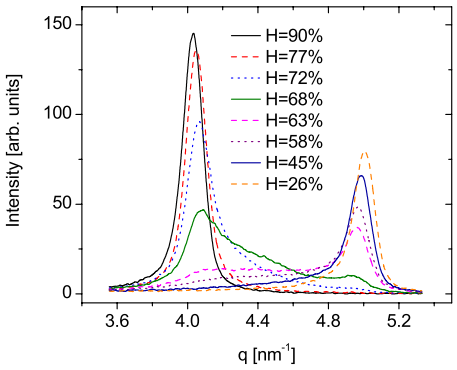

FIG. 8. (Color online) The azimuthally integrated and background-subtracted raw data from the 2D diffractograms in Fig. 6. Notice that the area of the pure 2 WL peak (left) is considerable larger than that of the pure 1 WL peak (right). This is due to various contributing scattering factors (layer structure factor and Lorentz-polarization factor).

dition, the amount of water in the clay, as well as nonclay contributions from air-scattering and scattering from the glass capillary, give rise to variations in the background shape and intensity, as a function of either time or spatial coordinates. Since small-angle scattering is known to follow a power law [22], a background power-law fit was subtracted from the raw data, thus producing radially normalized intensity plots [Fig. 8].

The total recorded scattering intensity has several contributions, and can be written as [8]

$$I(\mathbf{q}) \propto |G(\mathbf{q})|^2 L_p(\mathbf{q}) \Gamma(\mathbf{q}), \tag{1}$$

where I is the measured intensity, G is the layer structure factor, L_p is the Lorentz-polarization factor, Γ is the interference function and $\mathbf{q}$ is the transferred momentum. We are interested in the dynamics of water intercalation, which is reflected only in the dynamics of the interference function. We therefore divide the integrated and subsequently background-subtracted data by the product of the layer structure factor and the Lorentz-polarization factor. The layer structure factor [23]

$$G_{00l}(q) = 2\sum_j n_j f_j \exp\left[\frac{-W_j q^2}{(4\pi)^2}\right]\cos(qz_j) \tag{2}$$

was calculated using the number of atoms n_j of type j, located at positions z_j in the NaFh unit cell [8] and tabulated values of the atomic scattering factors f_j [24,25] and Debye-Waller factors W_j [23]. In the Lorentz-polarization factor ($L_p = 2P/\sin 2\theta \sin^\beta \theta$) [26], our unpolarized laboratory source has a polarization factor $P=(1+\cos^2\theta)/2$. For the exponent β, we used a mean value of $\beta=0.96$ for both hydration states, based on values obtained from an experiment performed on the same sample [8].

The resulting profile is that of the interference function, $\Gamma(q)$, whose peak positions in our q-range correspond to the interlayer spacing between the crystalline platelets. We have also observed that during hydration, a substantial amount of scattered intensity appears between the Bragg peak positions of pure 1 WL and 2 WL states (see Figs. 7 and 8). This is a well-known signature of disordered or mixed intercalation, a two-state coexistence that is often referred to as the transient Hendricks-Teller mixed-intercalation state [27]. Since the mixed intercalation is not the focus of the present work, we remove these contributions by fitting the interference function to pseudo-Voigtian functions [see Fig. 7(b)]. Only the q-regions containing pure Bragg peaks were used for the fitting, i.e., the intensity at q-values lower than the maximum intensity for the 2 WL peaks, and the intensity at higher q for the 1 WL peaks. As the pseudo-Voigtian is a linear approximation to the convolution of a Gaussian and Lorentzian function, it combines the peak broadening contributions from the instrumental resolution and particle thickness. For this experiment we are not so interested in the peak widths, but use the fact that the pseudo-Voigt is known to be a good description of experimental peak shapes [28,29]. The interlayer repetition distance of the clay particles, (d_{001}), is thus found from the peak momentum transfer obtained in the fitting (q_{001}) by the relation $d_{001}=2\pi/q_{001}$.

IV. RESULTS AND DISCUSSION

A. Bragg scattering vs humidity

As mentioned in Sec. I, hydration transitions correspond to drastic changes in the molecular packing inside the clay nanopores, but more subtle changes to this molecular packing can occur outside of the particular thermodynamic conditions that trigger the transitions. We have observed one such phenomenon in the form of small variation in the d-spacing within a given hydration state, as a function of the surrounding humidity level. The change is due to an exchange of water molecules between the mesopores and nanopores, which increases the packing of water molecules within the clay gallery to some extent [19], without triggering the overall revolution in the packing that is characteristic of the transition.

We recorded this change in d-spacing as a function of relative humidity, yielding the plot shown in Fig. 9. The two d-spacing plateaus in the plot represent two different hydration states: the plateau at $\approx$15.5 Å corresponds to the dihydrated state, while the other plateau at $\approx$12.5 Å corresponds to monohydration [8]. Notice that the exact value of these separations differ somewhat depending on the origin of the clay and the procedure of processing, hence values given in the literature can vary somewhat.

Except very close to the hydration transition at $H \approx 60-65\%$, there does not appear to be any major changes in the d-spacing within a given hydration state. However, by carefully varying the humidity in only one direction at the time, and plotting the data as in Fig. 9(b), a systematic change in the d-spacing magnitude on the order of approximately 0.3–0.4 Å ($\approx$2–3%), is observed away from the hydration transition. This phenomenon has previously been investigated in other swelling clays, both theoretically [18,30,31] and experimentally [32–34], but has to our knowledge never been mapped so thoroughly as in Fig. 9. Our method of varying the humidity in small steps using a pumped humidity regulator reveals that the d versus H rela-

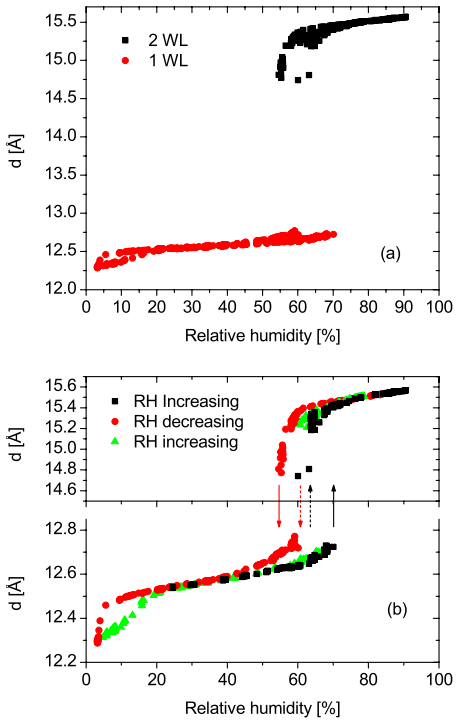

FIG. 9. (Color online) (a,b) d-spacing as a function or relative humidity. (b) The plot reveals a hysteretic behavior at the transitions from a monohydrated state (1 WL) to a dehydrated state (0 WL) as well as between the monohydrated and dihydrated (2 WL) states. The ranges of relative humidity for which transitions between the monohydrated and the dihydrated states occur are indicated by arrows: dotted line—transition initiates; solid line—transition ends.

tion is smooth and systematic, a phenomenon that we will utilize in Sec. IV B below.

Recording of the data in Fig. 9(b) was started at ambient humidity ($H \approx 25\%$) and gradually increased in small steps (black squares). At $H \approx 64-65\%$, a transition to the dihydrated state starts. This is seen from the appearance of d-spacings values at ≈ 15.2 Å (in fact, small 2 WL peaks or shoulders appeared a bit prior to this humidity value, cf. Fig. 8, but they were so small that fitting was not possible). The transition is complete at $H \approx 68-70$ %, seen by the fact that there are no more fitted monohydrated states. After the transition, the d-spacing curve follows a steady increase.

At $H \approx 92\%$ we moved from a steady increase of humidity to a gradual decrease (red circles). The transition back to a monohydrated state first initiates at $H \approx 60-61\%$, and completes at $H \approx 56-57$ %. Hence, the transition is evidently *hysteretic*, with a hysteretic width of approximately 11–14 %. After the transition to the monohydrated state, the decrease is again continuous until approaching what appears to be yet another hysteresis initiation at $H < 4\%$. This would be the transition to a dehydrated state (0 WL). However, at this particular temperature and with our system's lower constraint for relative humidity ($\approx 3\%$), we are only just out of range to complete the transition. We maintained the system at the lowest attainable humidity value for a longer period of time without seeing any effect, which ensured that equilibrium was reached.

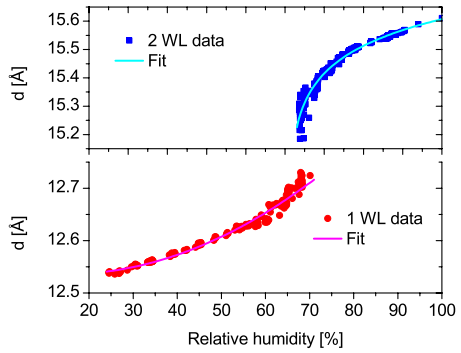

FIG. 10. (Color online) Function fit of $d(H)$ applied to the black squares and green triangles in Fig. 9(b) (gradually increasing humidity).

Finally, the humidity was once again increased in small steps (green triangles). Due to hysteretic behavior also for the dehydrated-monohydrated transition, the curve meets with the initial curve (black squares) only after the humidity has been increased to $H \approx 20\%$. Above this value however, the curves coincide almost perfectly in following the steady increasing plateaus of the stable hydrated states. We consider this an evidence of reproducibility, which furthermore justifies using the d-spacing as an indirect measure of the humidity level, as presented in the data treatment that follows. In order to extract an expression for the d-spacing parameter as a function of humidity, we performed a polynomial ("spline") fit to the data sets obtained from gradually increasing the humidity in Fig. 9(b). The fit and the data points used are displayed in Fig. 10. Note that the two rightmost points in the 2 WL curve in Fig. 10 have been added to the data from another experimental run where the humidity was increased all the way to 100%.

From the range of relative humidity values for which the transition from the monohydrated to the dihydrated state occurs, we can estimate a threshold humidity value that corresponds to the transition between the two states for increasing humidities. We choose the middle value between where the transition initiates and where it has completed and estimate the threshold to $H_{\text{threshold}} = 67.5\%$.

B. Humidity transport

To study water transport in a one-dimensional humidity gradient through a capillary filled with a powder clay specimen, we employed the experimental setup presented in Sec. II D. In Fig. 11 we have plotted the evolution in d-spacing as a function of time for twenty-five spatial coordinates in the sample. $x=0$ corresponds to the position of the capillary end exposed to humid air.

1. Relative humidity vs time

In the peak displacement experiment presented in Sec. IV A, we obtained a fitted function $d(H)$ (see Fig. 10) that gives the d-spacing of NaFh as a function of relative humidity (valid for a temperature of 15 °C). From the experimental data presented in Fig. 11 we have obtained the d-spacings at various spatial coordinates of the quasi one-dimensional

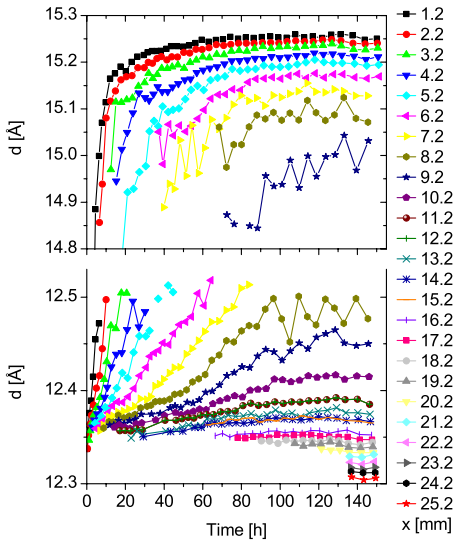

FIG. 11. (Color online) d-spacing as a function of time for 25 spatial coordinates in the quasi one-dimensional sample, separated by 1.0 mm. $x=0$ corresponds to the humid end of the sample.

sample as a function of time, $d(x,t)$. Hence we can relate the two types of information and use the measured quantity $d(x,t)$ to estimate at each position x the humidity content as a function of time. In doing so, we assume the H versus d relation to be the same during dynamic water transport as it was in the quasistatic $d(H)$ calibration experiment. We believe this estimate to be satisfying, as water transport is rather slow (days/cm) while the d spacing was seen to stabilize in less than 30 min when varying the humidity. The result of the conversion from d-spacing to humidity is shown in Fig. 12, along with a fit by a stretched exponential,

$$H_x(t) = H_x(t=\infty) \cdot \left(1 - \exp\left[-\left(\frac{t}{\tau_x}\right)^{\beta_x}\right]\right). \tag{3}$$

In spite of the approximations and assumptions employed in generating the plots shown in Fig. 12, the curves show evidence of a systematic behavior that substantiates the applied methods. There are some minor irregularities though; in particular we note that the curve fits to the spatial positions that

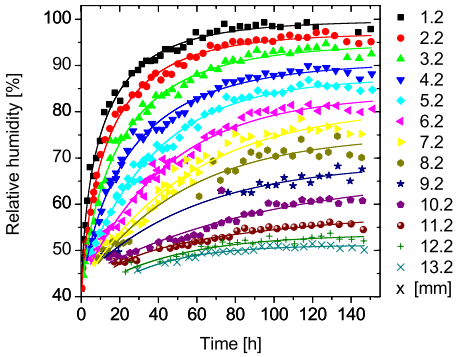

FIG. 12. (Color online) Water ingress (relative humidity) plotted as a function of time. Each curve represents a spatial position x of the sample; $x=0$ defines the sample-humidity reservoir interface. The curves are fits to the data by a stretched exponential [Eq. (3)].

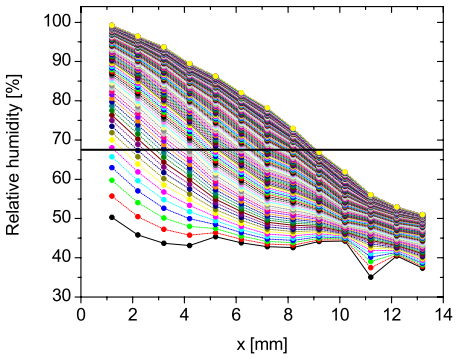

FIG. 13. (Color online) Water ingress (relative humidity) plotted as a function of position. Each curve represents a different time, one for each hour starting at 1 h (lower black, solid-drawn line). Every tenth curve is drawn as a thick, solid-drawn line corresponding to an increment of 10 h. The horizontal black line represents the intercalation threshold humidity level (67.5%) at which the intercalation transition occurs.

approach the transition threshold value of $H \approx 67.5\%$ as t goes to infinity are not very reliable due to the lack of data points. This concerns mostly the fits corresponding to spatial positions $x=7.2$ mm, $x=8.2$ mm, and $x=9.2$ mm.

2. Relative humidity vs position

The particular functional form used to fit the data points in Fig. 12 [a stretched exponential, see Eq. (3)], has within the context of our analysis no physical significance, but we can use it to perform the conversion $H_x(t) \rightarrow H_t(x)$. In other words we can get relative humidity profiles as a function of ingress x for selected times during the water transport. In Fig. 13 this is shown for a time step of 1 h, starting from $t=1$ h and going up to $t=45$ h. Every tenth curve, starting with $t=1$ h is represented by a thick unbroken line, whereas the intermediate times are shown as thin, dotted curves. For the earliest time curves ($t<10$ h), there are irregularities near $x=11$ mm that smooth out in time. This is either due to an initial heterogeneity in the clay sample, or to scarceness of data points at initial times far from the injected humidity, or probably to the superposition of these two effects. Note that the latter aspect was intentional, as we found it more important to map the rapid increase of humidity close to the wet side.

The humidity profiles shown in Fig. 13 have a shape characteristic of a diffusion process. All profiles seem to approach a lower bound of approximately 40% relative humidity, which is due to the ambient humidity present in the sample before starting the experiment.

From Fig. 13 we may obtain information on the propagation of the intercalation *front*. We define this as the position of the most advanced point in the sample (as a function of time) that has reached the threshold humidity value between the monohydrated and dihydrated states. In this context it therefore suffices to find the intersection of the constant line of the threshold value, $H_{\text{threshold}} \approx 67.5\%$, with each curve of Fig. 13. The point of intersection gives the time t for which the intercalation front has reached the given position x. A

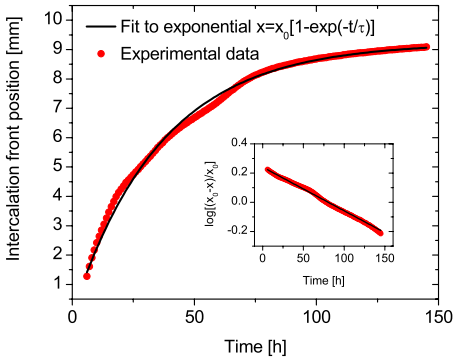

FIG. 14. (Color online) The data points shown are the intercalation front extracted from Fig. 12, along with a functional fit to an exponential (see figure legend) where $x_0=(9.22\pm0.05)$ mm and $\tau=(36.2\pm0.6)$ h. The inset is a semilog plot indicating the suitability of the exponential.

plot of the intercalation front's position in time is shown in Fig. 14.

3. Scaling of the humidity fronts

The one-dimensional diffusion equation, assuming a diffusion coefficient D that is a function of concentration only, is a nonlinear partial differential equation [35] in the form

$$\frac{\partial W}{\partial t}=\frac{\partial}{\partial x}\left[D(W)\frac{\partial}{\partial x}W(x,t)\right], \tag{4}$$

where W is the mass density of the diffusing material, D is the diffusion coefficient, and x and t are the spatial and time coordinates, respectively.

In our experiment, water diffuses through a highly porous medium packed in a thin and long glass capillary. Consequently, we consider the diffusion to be one-dimensional from a macroscopic point of view. Assuming a semi-infinite solid at $x\geq0$, in contact with a water reservoir located at $x<0$, the boundary conditions can be expressed as

$$W(x=0,t>0)=W_0,$$

$$W(x>0,t=0)=W_1. \tag{5}$$

A useful mathematical technique in studying some of classes of diffusion processes is the application of similarity transformations, such as Boltzmann's transformation

$$\eta=\frac{x}{t^{1/2}}. \tag{6}$$

This transformation is only applicable to solving Eq. (4) with initial and boundary conditions [Eq. (5)] if: (i) the initial and boundary conditions are expressible in terms of η alone, and if (ii) D is a function of W only [35]. Our method of circulating humid air on one side of the capillary and dry air on the other was intended to fulfill these conditions, provided that the tube be long enough for the semi-infinite medium assumption to be valid. However, the initial lowering of the sample temperature (on which the water vapor saturation pressure is strongly dependent) leads to an initial relative humidity of about 40%, prior to time $t=0$, at which the gradient is imposed on it (see Fig. 13). This means that the humidity in the sample at time $t=0$ is 40%, while that imposed at the dry end of the sample at later times is close to 0%. Consequently, in addition to a wet front diffusing into the capillary, there is also a simultaneous and opposite dry front diffusing from the other side. Strictly speaking, the boundary conditions cannot be formulated as a function of the sole η, which means that the use of the Boltzmann transform is not strictly justified. A compromise which still allows us to perform the transform, albeit with poorer precision, is to consider the diffusion only for short times, and close to the wet side: we only consider a region in time and space for which (i) the other end of the tube is far enough so that it can be considered at infinity, and (ii) the dry front that propagates from the other end is not felt. With this assumption, the appropriate initial and boundary conditions corresponding to those expressed in Eq. (5) are

$$W(\eta=0)=W_0,$$

$$W(\eta\to\infty)=W_1. \tag{7}$$

These approximate boundary conditions are functions of the scaling variable η alone. Besides, the diffusion equation can be expressed in terms of this sole variable. Thus, a universal behavior is to be expected for all values of x and t when the normalized concentration profiles, W/W_0, are plotted as a function of the scaling variable, η.

In the case of anomalous diffusion, the transport process can be described [36] by an equation,

$$\frac{\partial W}{\partial t}=\frac{\partial}{\partial x}\left[D(W,t)\frac{\partial}{\partial x}W(x,t)\right], \tag{8}$$

that resembles Eq. (5) but incorporates a diffusivity $D(W,t)$ that varies explicitly with time. If the diffusivity is taken to be a separable function of W and t, i.e., $D(W,t)=\gamma(t)\delta(W)$, scaling similar to the Boltzmann case above is obtained provided that η is substituted with $\xi=x/\tau^{1/2}$ [36], where

$$\tau=\int_0^t\gamma(t')dt'. \tag{9}$$

The typical distance traveled over a time duration τ scales as $\tau^{1/2}$. In the cases where this transport is slower than the usual $t^{1/2}$ scaling, the transport process is characterized as subdiffusive. For our sample, an explicit time dependence of the diffusivity could be related to changes in the pore structure, which makes anomalous diffusion likely in this type of material. Subdiffusive behavior has been observed in zeolites [37,38], which are close to clay minerals in terms of structural properties.

In Fig. 15 we have scaled the concentration profiles of Fig. 13 as a function of η. According to the arguments above, this should collapse all humidity profiles on a master curve if the transport process is normally diffusive. By also attempting to scale the profiles as $\xi=x/t^{a/2}$, where a is a constant close to 1, we tested for small deviations from normally diffusive behavior. The value of a that provided the best collapse of our measured profiles was found to be a

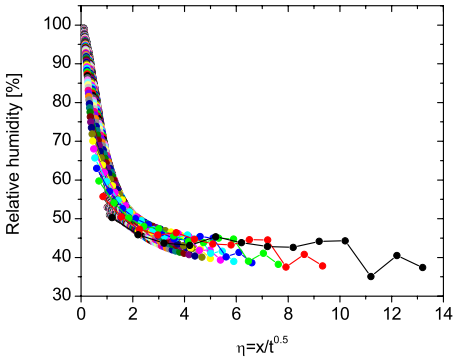

FIG. 15. (Color online) Data collapse of the obtained concentration profiles, obtained at times from 1 h $\leq t \leq$ 145 h. The data are plotted as a function of $\eta = x/t^{1/2}$.

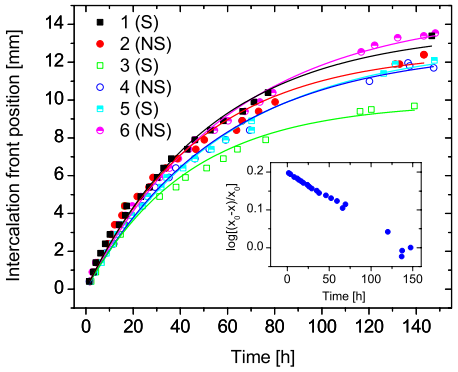

FIG. 16. (Color online) The calculated intercalation front for all six capillaries used to test the effect of capillary forces. Data from the silanized capillaries are labelled (S), whereas data from nonsilanized (untreated) capillaries are labelled (NS). The function fit is a standard exponential equal to the one performed in Fig. 14. The inset is a semilog plot of the data for capillary 4, indicating the suitability of the exponential fit.

$\approx 1.0 \pm 0.1$. We attribute the poor quality of the scaling to the limitations imposed by the not fully proper boundary conditions met in the experiment, as explained above. Hence we cannot infer the value for a to a precision better than 0.1. We conclude that the water transport resulting from the humidity gradient imposed on our quasi-one-dimensional powder sample of NaFh at constant temperature is described by a diffusion process that is either normal or weakly anomalous. As this transport experiment is presented here as an example of what the $d(H)$ relation found in Sec. IV B 2 can be useful for, we do not go into more details in the present study. In order to determine whether there is any anomalous behavior in the diffusion of water vapor through the system, other experiments, with boundary conditions more suitable for transport, are needed.

4. Transport in hydrophobic vs hydrophilic tubes

By simultaneously studying the humidity transport through hydrophobic and hydrophilic glass capillaries, we investigated whether glass wall capillary forces could influence the transport process. In order to study six capillaries simultaneously and still have an acceptable signal to noise ratio, we focused only on mapping the intercalation fronts ingressing into the samples, and not on acquiring humidity profiles similar to Fig. 13. To obtain curves of the intercalation fronts' position as a function of time, we first performed the same data processing as for the single capillary case (Sec. III), and then normalized the areas of the recorded 1 WL and 2 WL peaks by their fully developed counterparts (i.e., the area of peaks for the pure intercalation states). The positions of the intercalation front as a function of time were then determined from the most advanced position at any given time where the ratio between the areas of the normalized 1 WL and 2 WL peaks were equal [10]. The resulting intercalation fronts for all six treated and untreated capillaries are shown in Fig. 16.

In the curves shown in Fig. 16, differences between and variations-among the curves are visible. There are several reasons that might explain them. A possible systematic explanation is the existence of gradients in the system, both in temperature and/or humidity and perpendicularly to the capillaries' length, that is, resulting in differences between the humidity- and temperature-boundary conditions met by the different capillaries. It seems reasonable that any such gradient would manifest itself by a systematic monotonic change in the curvature of the intercalation fronts from capillary 1 to 6. As seen in Fig. 16, it is not the case. Other factors that could affect the rate of transport are condensation on the sample holder, differences in packing of the power, and differences in capillary radius. In any case, the differences between the plots do not seem to be in any way correlated with the hydrophilicity of the glass surfaces. In other words, the figure shows no systematic difference between the behaviors of silanized vs nonsilanized samples, which allows us to conclude that film flow on the capillary walls due to the hydrophilicity of the glass capillaries does not have a significant effect on water transport, in our diffusion experiments.

V. CONCLUSION

We have shown that under varying humidity, there are systematic changes in the interlayer space of NaFh crystallites within a given hydration state. The small ($\approx$0.3 Å) shifts are reproducible and on the order of 2–3 % for the mono- and dihydrated states. The results are in accordance with previous experiments, but to our knowledge the relation between d-spacing and relative humidity has never been proven to be as smooth and continuous, nor as reproducible, as our results show. Our method of mixing dry and humid air in a controlled manner enabled a continuous change in the relative humidity imposed on the clay sample, as opposed to the often used method of enclosing dry samples in chambers with saturated salt solution. The systematic behavior is consistent with a Monte Carlo simulation by Boek *et al.* [18] on Wyoming montmorillonite, which showed that a gradual increase of water molecules in the interlayer space results in a monotonic widening of the layer spacing, with sharp steps occurring only when additional water layers starts to form.

Our detailed mapping of the relative humidity-controlled d-spacing, together with its reproducibility and reliability has enabled the use of interlamellar repetition distance as a mea-

sure of the local humidity surrounding the clay particles. We have demonstrated an application of this method to the monitoring of humidity diffusion along a quasi-one-dimensional weakly hydrated mesoporous clay sample. Our experimental conditions made further analysis of the data complicated, but under certain simplifying assumptions we were to some extent able to scale the profiles using the Boltzmann transformation of the diffusion equation. The measured diffusive behavior is either normal or possibly weakly anomalous.

From an estimate of the threshold humidity value that corresponds to the transition from the monohydrated to the bihydrated intercalation states, we have inferred the ingress of the intercalation front into the sample as a function of time: the front progresses according to an exponential function of time. We have also tested for potential contributions to water transport caused by the hydrophilic nature of the glass capillary walls, and found no systematic difference.

In order to improve our analysis of water diffusion using this technique, a modified experimental setup, possibly using synchrotron x rays for better statistics, and dehydrating the clay before imposing the gradient, is planned as future work.

ACKNOWLEDGMENTS

This work has been supported by the Research Council of Norway (NFR) through the NANOMAT and the FRINAT programs. H.H., J.O.F., and Y.M. acknowledge support from the Aurora French-Norwegian collaboration program for travel between France and Norway (French Aurora Grant No. 18810WC, NFR Grant No. 187697/V11). Y. M. also acknowledges support from CNRS under a French-Norwegian PICS project. The authors thank B. Sandnes for very helpful discussions.

[1] C. Durand, T. Forsans, C. Ruffet, A. Onaisi, and A. Audibert, Rev. Inst. Fr. Pet. **50**, 187 (1995).
[2] A. Khaldoun, P. Moller, A. Fall, G. Wegdam, B. De Leeuw, Y. Meheust, J. O. Fossum, and D. Bonn, Phys. Rev. Lett. **103**, 188301 (2009).
[3] P. Landais, Appl. Clay Sci. **26**, 1 (2004).
[4] A. Busch, S. Alles, Y. Gensterblum, D. Prinz, D. N. Dewhurst, M. D. Raven, H. Stanjek, and B. M. Krooss, Int. J. Greenh. Gas Control **2**, 297 (2008).
[5] J. O. Fossum, Physica A **270**, 270 (1999).
[6] F. Bergaya, B. K. G. Theng, and G. Lagaly, *Handbook of Clay Science* (Elsevier, Amsterdam, 2006).
[7] G. J. da Silva, J. O. Fossum, E. DiMasi, and K. J. Maloy, Phys. Rev. B **67**, 094114 (2003).
[8] G. J. da Silva, J. O. Fossum, E. DiMasi, K. J. Maloy, and S. B. Lutnaes, Phys. Rev. E **66**, 011303 (2002).
[9] K. D. Knudsen, J. O. Fossum, G. Helgesen, and M. W. Haakestad, Physica B **352**, 247 (2004).
[10] G. Lovoll, B. Sandnes, Y. Meheust, K. J. Maloy, J. O. Fossum, G. J. da Silva, M. S. P. Mundim, R. Droppa, and D. M. Fonseca, Physica B **370**, 90 (2005).
[11] Y. Méheust, K. D. Knudsen, and J. O. Fossum, J. Appl. Crystallogr. **39**, 661 (2006).
[12] P. D. Kaviratna, T. J. Pinnavaia, and P. A. Schroeder, J. Phys. Chem. Solids **57**, 1897 (1996).
[13] E. DiMasi, J. O. Fossum, T. Gog, and C. Venkataraman, Phys. Rev. E **64**, 061704 (2001).
[14] D. A. Laird, Clays Clay Miner. **44**, 553 (1996).
[15] N. T. Skipper, K. Refson, and J. D. C. Mcconnell, J. Chem. Phys. **94**, 7434 (1991).
[16] N. T. Skipper, P. A. Lock, J. O. Titiloye, J. Swenson, Z. A. Mirza, W. S. Howells, and F. Fernandez-Alonso, Chem. Geol. **230**, 182 (2006).
[17] G. Sposito, N. T. Skipper, R. Sutton, S. H. Park, A. K. Soper, and J. A. Greathouse, Proc. Natl. Acad. Sci. U.S.A. **96**, 3358 (1999).
[18] E. S. Boek, P. V. Coveney, and N. T. Skipper, J. Am. Chem. Soc. **117**, 12608 (1995).
[19] R. P. Tenorio, L. R. Alme, M. Engelsberg, J. O. Fossum, and F. Hallwass, J. Phys. Chem. C **112**, 575 (2008);R. P. Tenorio, M. Engelsberg, J. O. Fossum, and G. J. da Silva, Langmuir **26**, 9703 (2010).
[20] A. Wexler, in *CRC Handbook of Chemistry and Physics*, 89th ed. (Internet Version 2009), edited by D. R. Lide (CRC Press; Taylor & Francis, Boca Raton, FL, 2009).
[21] Sigma-Aldrich Norway AS (unpublished).
[22] J. D. F. Ramsay, S. W. Swanton, and J. Bunce, J. Chem. Soc., Faraday Trans. **86**, 3919 (1990).
[23] G. W. Brindley and G. Brown, *Crystal Structures of Clay Minerals and Their X-ray Identification* (Mineralogical Society, London, 1980).
[24] P. J. Brown, A. G. Fox, E. N. Maslen, M. A. O'Keefe, and B. T. M. Willis, *International Tables for Crystallography* (Springer, New York, 2006), Vol. C.
[25] C. Hammond, *Introduction to Crystallography* (Oxford University Press, Oxford, 1990).
[26] D. M. Moore and R. C. Reynolds, *X-ray Diffraction and the Identification and Analysis of Clay Minerals* (Oxford University Press, Oxford, 1997).
[27] S. Hendricks and E. Teller, J. Chem. Phys. **10**, 147 (1942).
[28] P. Thompson, D. E. Cox, and J. B. Hastings, J. Appl. Crystallogr. **20**, 79 (1987).
[29] G. K. Wertheim, M. A. Butler, K. W. West, and D. N. Buchanan, Rev. Sci. Instrum. **45**, 1369 (1974).
[30] T. J. Tambach, E. J. M. Hensen, and B. Smit, J. Phys. Chem. B **108**, 7586 (2004).
[31] O. Vidal and B. Dubacq, Geochim. Cosmochim. Acta **73**, 6544 (2009).
[32] M. H. Fu, Z. Z. Zhang, and P. F. Low, Clays Clay Miner. **38**, 485 (1990).
[33] R. Calvet, Ann. Agron. **24**, 77 (1973).
[34] K. Norrish, Discuss. Faraday Soc. **18**, 120 (1954).
[35] J. Crank, *The Mathematics of Diffusion* (Clarendon Press, Oxford, 1975), p. VIII.
[36] D. A. Lockington and J. Y. Parlange, J. Phys. D **36**, 760 (2003).
[37] E. N. de Azevedo, P. L. de Sousa, R. E. de Souza, M. Engelsberg, M. de N. do N. Miranda, and M. A. Silva, Phys. Rev. E **73**, 011204 (2006).
[38] E. N. de Azevedo, D. V. da Silva, R. E. de Souza, and M. Engelsberg, Phys. Rev. E **74**, 041108 (2006).